Precision Engineering 71 (2021) 119–129

Contents lists available at ScienceDirect

Precision Engineering

journal homepage: http://www.elsevier.com/locate/precision

Highly efficient smoothing of Inconel 718 via electrochemical-based isotropic etching polishing

Khan Muhammad Ajmal [a], Rong Yi [a], Zejin Zhan [a], Jianwei Ji [a], Xinquan Zhang [b,**], Hui Deng [a,*]

[a] Department of Mechanical and Energy Engineering, Southern University of Science and Technology, No. 1088, Xueyuan Road, Shenzhen, Guangdong, 518055, China
[b] School of Mechanical Engineering, Shanghai Jiao Tong University, Shanghai, 200240, China

ARTICLE INFO

Keywords:
Inconel 718
Polishing
Electrochemical etching
Roughness
Etching anisotropy

ABSTRACT

For the highly efficient and versatile polishing of metals, isotropic etching polishing (IEP), which is based on the merging of isotropic etching holes, has been developed. In this study, the feasibility and mechanism of isotropic etching polishing of nickel-based superalloy Inconel 718 (IN718) and the polishing characteristics have been studied. The potentiodynamic experiments revealed similar trends of the cathodic, passive, second passivation, and transpassive regions in all the electrolytes, while the corrosion susceptibility of IN718 successively decreased with the increasing H_2SO_4 concentration in the electrolyte. The etching anisotropy of the IN718 precipitated with different phases can be experimentally transmuted to isotropic etching by modulating the electrolyte concentration and keeping electrolyte temperature equal or above the room temperature. Because of the positive correlation of the etching current with isotropic holes density and diameter, etching at higher currents is promoted for the rapid and proficient polishing. The surface evolution mechanism during IEP has been confirmed. The surface roughness initially increased due to the formation of etching holes, then decreased abruptly owing to the rapid merging of etching holes and finally achieved a smooth surface. The wet grounded surface of IN718 with a roughness of Sa 62.7 nm has been transformed into a mirror-like smooth surface with a roughness of Sa 0.86 nm within 300 s of IEP at optimized conditions and a high MRR of 2.73 mm^3/min has been achieved.

1. Introduction

Aerospace and automotive are amongst the fastest-growing industries of the modern era that put forward an insistent demand for high-temperature-resistant materials with improved mechanical properties and performance. Nickel-based alloys (Inconel 625 and 718) offer excellent mechanical properties and higher thermal strength even under worse operating conditions than their coetaneous metals and alloys [1]. For example, the IN718 crystal structure can withstand high working temperatures (~650 °C). Du et al. [2] reported further improvement in the thermal strength of IN718 by slightly adjusting the chemical composition. Besides, IN718 exhibits excellent mechanical properties such as high strength, microstructure durability, oxidation resistance, good weldability, and so on. Because of the aforementioned mechanical properties, approximately 40–50% weight of the jet engine and different components such as disks, shafts, flanges, etc., functioning in the hot sections of nuclear power plants and gas turbines are made of IN718 [3,4].

Although, excellent mechanical properties of IN718 make it worthwhile for many industrial applications, low thermal conductivity, work hardening effect, high strength and hardness have limited its machining efficiency, consequently increasing the processing cost [5]. Considering the increasing demand for industrial materials with enhanced individual component performance and efficient mechanical functioning, metals with mirror-like shining surfaces and minimum roughness are highly desired. Simultaneously, because of the inevitable importance of component polishing in general and exclusively at the application stage, surface polishing techniques should be energy-efficient, cost-effective, and adaptable to complex component designs. At present, conventional surface polishing techniques incorporate mechanical polishing (MP) or chemical mechanical polishing (CMP). However, a mechanically polished surface may contain subsurface damages (SSD), micro-scratches, embedded abrasives, and strains [6]. Mechanical actions are significantly reduced in CMP, as the chemical reaction of the oxidants and surfactants in a slurry with surface softens the uppermost layer of the substrate [7]. Subsequently, a mild mechanical action of abrasives

* Corresponding author.
** Corresponding author.
E-mail addresses: zhangxinquan@sjtu.edu.cn (X. Zhang), dengh@sustech.edu.cn (H. Deng).

https://doi.org/10.1016/j.precisioneng.2021.03.005
Received 19 October 2020; Received in revised form 9 February 2021; Accepted 13 March 2021
Available online 20 March 2021

removes the squashy products formed on the surface. However, subsequent hazardous waste from CMP is troublesome, requiring huge research and capital investment to develop environment friendly slurries [8]. Abrasive jet machining (AJM) and water jet machining (WJM) are also mechanical based polishing techniques that utilize abrasive particles driven by a gas stream, which ejects through a nozzle at very high speed (200–400 m/s) and subsequently interact with the substrate [9]. However, AJM and WJM cannot polish complex parts especially with inner features.

Advanced metal polishing techniques such as multi-jet polishing (MJP) [10], ion beam polishing (IBP) [11], laser polishing (LP) [11], and magneto-rheological polishing (MRP) [12], operated by remote energy sources, are also coming to prominence. These techniques are widely used to process different metals and alloys, such as the polishing of TC4 titanium with high current pulsed electron beam [13], and IN718 with electric discharge and laser beam [14]. Wang et al. [10] studied MJP both computationally and experimentally and found that a large surface area of the MJP is feasible to achieve high MRR and enhanced polishing efficiency. In LP, a high energy laser irradiating the metallic substrates generates a facile layer of the molten metallic pool, which relocates from protrudes to the valleys, ultimately resolidifies and develops a smooth glossy surface [15]. Zhihao et al. investigated the laser polishing of additively manufactured IN718, and results show that the original surface roughness of 7 μm was reduced to 0.1 μm [16]. However, high energy processing techniques offer very slim beam dimensions, and induce heat-affected zones (HAZ) on the substrate micro-structures that need to be mitigated by post-processing [17].

Electrochemical polishing (ECP) is a highly endorsed metal finishing technique because of the obvious advantages such as simple and stress-free operation, independence from substrate shape because of aqueous working media, and extensive application spectrum including soft metals and hard alloys [18]. Based on the ECP, the manufacturers can shape conductive materials, such as the fabrication of sub-10-nm tungsten tips with a long taper and a large shank by lamellae and inverse lamellae drop-off etching [19], and the generation of uniform surface finish without bothering the bulk properties of the substrate [20]. Different researches discussed the controlling parameters and the coupling of ECP with additional energy sources such as ultrasonic cleaning and magnetic field to achieve the nano-finishing of metals [18,21]. According to the electrochemical polishing of IN718 performed by using a rotating disc electrode in $HClO_4$–CH_3COOH electrolyte, polishing effects such as leveling without brightening, leveling and brightening, and the matt and gray surface were obtained with different concentration of $HClO_4$ in the electrolyte [22]. However, many large size Nb rich particles were not leveled in this process. Likewise, a slurryless electrochemical mechanical polishing (ECMP) of single-crystal 4H–SiC was conducted by developing a balance between the anodic oxidation and the polishing rate of the oxide layer [23]. Despite a long history, the basic understanding of ECP is still very weak, while the most widely accepted theory to understand the mechanism of ECP was proposed by Jacquet [24]. According to Jacquet, a passivation layer develops on a metallic substrate immersed in an electrolyte, the thickness of the layer depends upon the initial surface quality of the substrate. Therefore, the metal dissolution rate is faster at the protrudes because of the thin passivation layer as compared to valleys. However, sometimes ECP results in the variable surface finish even under the same operating conditions [20]. In addition, the formation of an electrically resistant passivation layer, especially in the presence of chromium, prevents the surface from dissolution during ECP [25]. And the high electrical resistance of the passivation layer results in considerable energy consumption [26]. Besides, finding appropriate electrolytes depending upon the nature of polishing material and troublesome optimization of the working parameters makes ECP further challenging [21].

Recently, Yi et al. [26] proposed a generic isotropic etching polishing (IEP) approach for metals and substantiated its feasibility theoretically and experimentally. According to the IEP, the anode potential breaks the passivation layer due to which isotropic etching holes are formed on the substrate. These isotropic etching holes grow in diameter and merge to create a smooth and shiny substrate surface. Apart from the electrochemical nature of both ECP and IEP, the IEP consumes less energy due to the breakdown of the passivation layer, while the surface roughness during IEP first increases and then decreases, which is entirely different from the ECP. Although the isotropy/anisotropy in etching polishing was discussed as a function of the electrolyte concentration, the temperature of the electrolyte is another crucial factor that may affect the formation of isotropic etching holes. Therefore, the experimental investigation of the electrolyte temperature effect on the etching anisotropy is very important. Moreover, the investigation of the formation and breakdown of a thin passivation layer on a substrate originally in the etching electrolyte can be a substantial evidence of the IEP mechanism. It is challenging for electrochemical techniques to polish a multiphase material, as each phase has different chemical-mechanical properties and variable dissolution rate [27]. IN718 is a multiphase nickel alloy (γ′, γ″, and δ) [16,28], precipitated additionally with metal carbides [29]. Therefore, the presence of different phases and metal carbides makes the IEP of IN718 immensely challenging.

Following established grounds, the present work is focused on the experimental investigation of IN718 surface evolution during IEP with an ultimate objective to achieve minimum surface roughness for the commercial applications of the nickel alloy. In addition, potentiodynamic measurements of IN718 in different electrolytes, the effect of electrolyte temperature on the etching anisotropy, and the formation of a thin passivation layer on IN718 are investigated. The surface morphology evolution, average surface roughness (Sa roughness), and the MRR as a function of the etching current are also studied.

2. Material and experiments

2.1. Chemical composition of IN718

The manufacturing process and the chemical composition of the alloys are very important to determine their mechanical properties. The chemical composition (wt%) of the IN718 used in this study was determined by the energy dispersive spectrometer (EDS) via a scanning electron microscope (SEM, 10 ZEISS Merlin). The chemical compositions determined from random locations on the substrate (Fig. 1(a and b)) are listed in Table 1. As evident from the difference in chemical composition, Fig. 1(a) represents the bulk of the IN718 [30], while the composition recorded from the massive particle in Fig. 1(b) illustrates the metal carbides (MC carbides, where M denotes metal and C denotes carbon). Having an insignificant component of the fundamental Ni element, the MC carbides are rich in Nb, Ti, and C, so Ghorbanpour et al. referred to them (Nb, Ti)C having Fm-3m unit cell [31]. The investigation of microstructural evolution in IN718 shows that although MC carbides have low volume fractions (~1.5%), the homogeneous distribution of MC carbides in IN718 is useful to control the grain size and badge the grain boundaries [32].

2.2. XRD and EBSD analysis

As investigated by the EDS, IN718 is a nickel-based superalloy having multi-element composition. These elements during the cooling process can precipitate fundamental γ matrix and different intermetallic phases such as γ′, γ″, δ, and MC carbides [16,33]. The X-Ray Diffraction (XRD) patterns of the raw and isotropically etched polished IN718 samples scanned by the Cu-K_α radiations at a step size of 0.02°, operating at 45 kV and 200 mA are shown in Fig. 2(a). According to XRD analysis, two different phases γ-(Ni-FCC) and γ″-(Ni_3Nb-BCT) are present in IN718, which is in accordance with Ref. [16]. Besides, the presence of different crystallographic faces (111, 200, and 220) and the attendance of the strongest peak of 111 at $2\theta = 43.44°$ belonging to the primary γ phase is also consistent with the standard XRD pattern of the nickel alloy

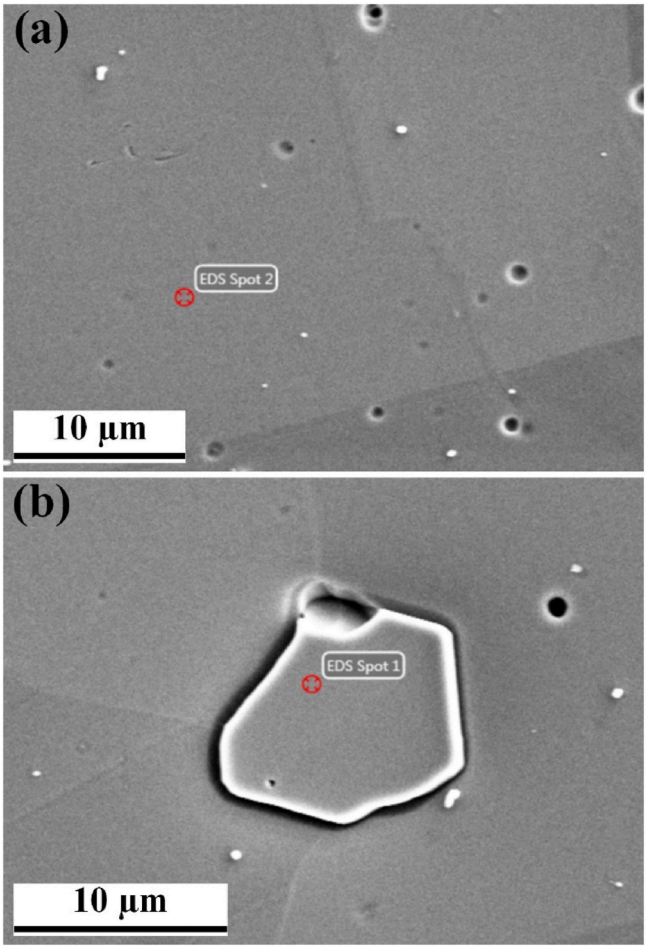

Fig. 1. SEM images for EDS analysis, IN718 alloy (a), and MC carbides (b).

Table 1
Chemical composition of the IN718 measured by EDS.

Element	Ni	Cr	Fe	Nb	C	Mo	Ti	Al
IN718 (wt%)	52.23	23.0	17.5	3.38	0.72	2.36	0.60	0.03
MC carbides (wt%)	0.79	0	0.53	84.83	4.81	0	9.07	0

IN718. It is to be mentioned that neither any other intermetallic phase such as γ′ or δ phase nor any phase shift was observed in the XRD spectra of polished IN718 compared with unprocessed sample spectra. The mechanical properties of IN718 are strongly dependent upon the concentration, size, and morphology of the γ″ phase [34]. However, unlike metallic nature and composition of precipitated phases, and different individual electrochemical dissolution rates make the electrochemical polishing of multiphase alloys challenging [27]. The intensity ratio of XRD peaks at 2θ = 43.44° and 50.56° for the polished sample is lower than the raw sample, which shows an apparent preferential dissolution of the γ phase. The primary γ phase in IN718 is dominant as compared to the intermetallic γ″ phase. Therefore, it is possible that the polishing exposed γ″ phase, and comparatively, a larger intensity is recorded during XRD characterization. However, the EBSD (Fig. 2(b)) and SEM images (Figs. 9 and 11) show no height difference between the grain boundaries.

The crystallographic textures and the grain shapes of the γ phase in polished IN718 were recorded by electron backscattered diffraction (EBSD) via SEM (EHT = 20 kV and step size = 0.6 µm), as shown in Fig. 2 (b). The average grain size in IN718, as measured by EBSD, is 13.2 µm.

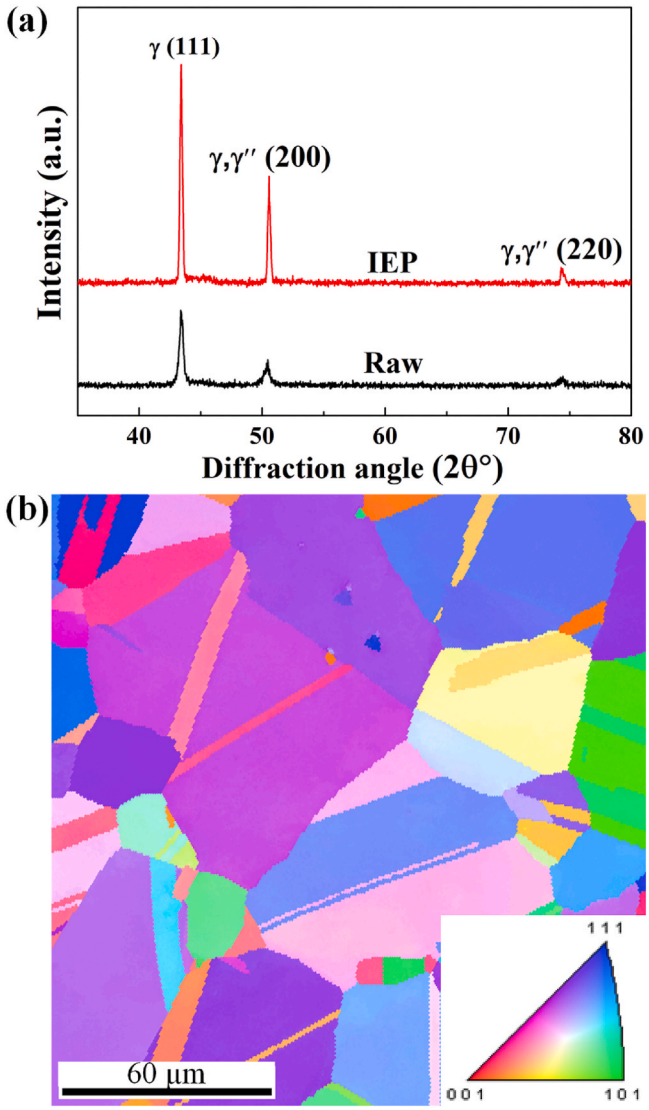

Fig. 2. XRD profiles (a) and EBSD map with inverse pole figure (IPF) of polished IN718 (b).

The overall grains pattern seems to be quite random, and very few grains can be seen in <101> and <001> direction. However, a slightly higher concentration of grains is aligned along <111> direction, which might be the heat flow and rolling direction adopted during the substrates manufacturing processes.

2.3. Experimental method

Commercially available disk-shaped IN718 substrates ($d = 15$ mm, $T = 3.5$ mm) were used for IEP. Before IEP, the IN718 substrates were finely grounded with wet 180-grit SiC sandpaper to remove the slicing marks. Subsequently, to eliminate contaminants, the substrates were ultrasonically cleaned in deionized (DI) water and ethanol absolute for 5 min each, respectively. The IEP was conducted in a glass beaker reaction cell where the IN718 as a working electrode was connected to the anode, while platinum plate (2 × 2 cm^2) as a counter electrode was connected to the cathode of the DC power supply (Keysight E3649A dual output), as shown in Fig. 3(a). The potential difference applied across the electrodes caused the etching current to pass through the electrolyte. The polishing electrolyte is composed of analytical grade sulfuric acid (H_2SO_4-97%) and methanol (CH_3OH-99.5%). The components of the electrolyte serve the following purposes: (i) anodic surface passivation

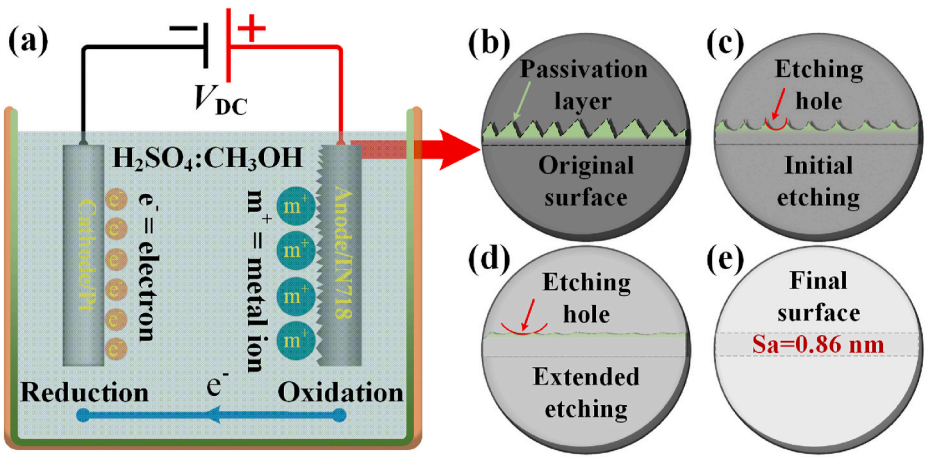

Fig. 3. Schematic of the experimental setup (a) and the principle of IEP (b–e).

and etching by H_2SO_4 [26], and (ii) destabilizing passivation layer by CH_3OH [35]. The overall reactions occurring in the reaction cell are as follows:

$$\text{Cathode: } 2nH_2SO_4 + 2ne^- \rightarrow nSO_2 + nSO_4^{2-} + 2nH_2O \quad (1)$$

$$\text{Anode: } 2M \rightarrow nM^+ + 2ne^- \quad (2)$$

where M is a general acronym denoting different metals present in the IN718. It is to be mentioned that the distance between electrodes was kept fixed at 50 mm, while the IEP was conducted at room temperature unless otherwise stated. A Teflon holder insulates the backend of IN718 substrate, and the IEP mechanism is exclusively performed on the front face, as described by the schematic shown in Fig. 3(b–e). Other than EDS and EBSD, the surface morphology of the IN718 was also captured by SEM, the Sa roughness by an atomic force microscope (AFM, Bruker Edge), and the MRR was determined from the before and after IEP mass difference of the substrate measured by a precision balance (Mettler Toledo, ME203).

3. Results and discussion

3.1. Potentiodynamic behavior of IN718

The potentiodynamic experiments were performed in three electrolytes with 10, 20, and 30 ml H_2SO_4 concentration in 100 ml methanol. The three channels of the conventional electrochemical workstation (CS350H) measurement system were connected to the reference electrode (Hg/H_2SO_4), cathode (Pt), and IN718 working as an anode. At first, the open circuit potential (OCP) was recorded for 10 min in each case to observe the stability of the working system. Followed by OCP, the potentiodynamic polarization experiments were conducted by automatically scanning 10 mV/s over a potential range of −2.5 to 3.5 V. The resulting curves show cathodic, active, passive, and transpassive regions, as shown in Fig. 4. On increasing H_2SO_4 concentration from 10 to 30 ml in 100 ml methanol, an increase in the critical current density (j_c = 1.34–1.71 mA/cm^{-2}) and a decrease in passive current density (j_p = 5.16–3.44 mA/cm^{-2}) was observed. The negative correlation of the two current densities is related to the increasing H_2SO_4 concentration in methanol, where the active anodic dissolution of Ni atoms resulted in higher j_c, while strong passivity endorsed by the rising water content in the passive region decreased j_p. Similar electrochemical behavior was also reported in a study investigating the electrochemical behavior of IN718 in acidic conditions [36]. The passivation region was witnessed in all three cases, where slight variations in the current densities might be related to the preferential phase dissolution and the occurrence of secondary passivation. The secondary passivation is a minor attribute of the

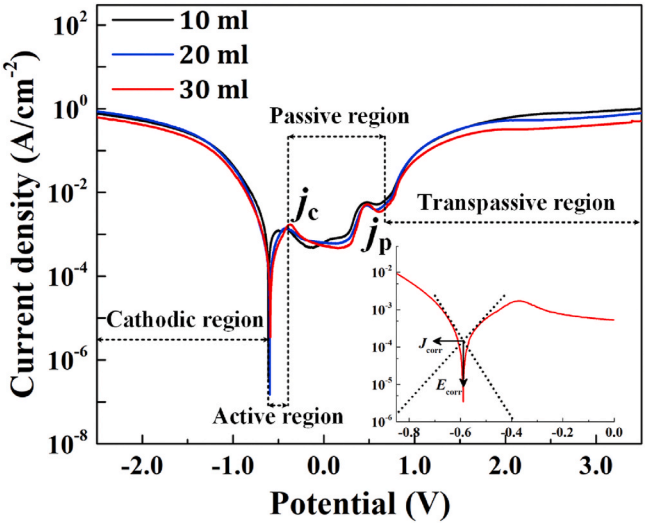

Fig. 4. The potentiodynamic response of IN718 as a function of the H_2SO_4 concentration in methanol.

Ni–Cr alloys, which is closely associated with the higher H_2SO_4 concentration in methanol [37,38]. The primary passivation is caused by NiO [39], while the secondary passivation occurs due to the formation of NiO_2 [40] by the following chemical reactions:

$$Ni + H_2O \rightarrow NiO + 2H^+ + 2e^- \quad (3)$$

$$NiO + H_2O \rightarrow NiO_2 + 2H^+ + 2e^- \quad (4)$$

Such a tendency of re-passivation might also be connected with the precipitation and dissolution influenced anodic reactions. Following the passivation layer breakdown, although a gradual increase in the current density was observed at higher electric potentials in all the cases, it was limited by the increasing H_2SO_4 concentration due to the decreasing electrolyte viscosity. Ultimately the minimum value of limiting current density was recorded for 30 ml H_2SO_4 concentration in 100 ml methanol. Besides, the corrosion performance of the IN718 was determined from the corrosion current density (J_{corr}) and corrosion potential (E_{corr}) corresponding to the intersection of the tangents to the cathodic and anodic wings of the Tafel plot, as shown in the inset of Fig. 4. It was observed that with increasing H_2SO_4 concentration from 10 to 30 ml in 100 ml methanol, the J_{corr} decreased (0.17–0.14 mA/cm^2), and E_{corr} became more positive (−0.61 to −0.59 V), indicating a better anti-corrosion performance of the IN718 in 30 ml H_2SO_4 concentration in

100 ml methanol. Moreover, it is to be mentioned that the minimum electric potential (1.63 V) during IEP was greater than the threshold potential (0.8 V) of the transpassive region, thus all the etching experiments were carried in the transpassive region.

3.2. Passivation layer breakdown

The IEP is based on the merging of isotropic etching holes formed after the breakdown of the passivation layer. Moreover, the passivation layer formed on the substrate immersed in the electrolyte is very thin, and the experimental observation of the breakdown site is challenging. Therefore, witnessing the existence of the passivation layer on the IN718 formed in the H_2SO_4 electrolyte [41], and the breakdown site of the passivation layer is important.

To investigate the presence of the passivation layer and the breakdown site, isotropic etching of IN718 was performed at 0.3 A for 80 s in an electrolyte having 20 ml H_2SO_4 concentration in 100 ml methanol. While the ultrasonic cleaning of the etched IN718 substrate in DI water and ethanol was intentionally avoided to keep the passivation layer intact after etching. Mishra [42], established that the development of the passivation layer is a characteristic of the Ni alloys containing sufficient Cr when exposed to a suitable environment, such as the H_2SO_4. It is because of the strong affinity of Cr for O, which leads to the formation of Cr_2O_3 on the IN718 substrate. Moreover, the presence of Mo in the alloy further retards local breach in the oxide film. Similar findings of the formation of NiO, Cr_2O_3, and Al_2O_3 during the oxidation of Ni alloys were also reported in Ref. [43]. Therefore, EDS analysis of the isotropically etched IN718 surface was performed before the ultrasonic cleaning, and the composition is listed in Table 2. Although the IN718 compositions presented in Tables 1 and 2 are quite similar, the supplementary attendance of O in the EDS analysis of isotropically etched IN718 surface without post etch ultrasonic cleaning strongly supports the metals oxides formation.

The passivation layer breakdown site and the intact passivation layer on the IN718 substrates without the ultrasonic cleaning can be seen in Fig. 5(a). Fig. 5(b) and (c) represents the laser scanning confocal microscope (LSCM, Keyence VK-X1000) images of the etching sites without and with ultrasonic cleaning, respectively. Moreover, the LSCM cross-sectional profiles of the passivation layer breakdown site without ultrasonic cleaning and the etching hole developed with ultrasonic cleaning are shown in Fig. 5(d). Despite the apparent difference in the geometries of the passivation breakdown site without ultrasonic cleaning and the etching hole that emerged with ultrasonic cleaning, their depths are relatively comparable. This is because of the etching at the optimized conditions, where the etching happens at the breakdown site under the intact passivation layer. Ultimately, the isotropic etching hole emerges after the intact layer is ultrasonically cleaned.

3.3. Etching anisotropy of IN718

The microstructural investigations of IN718 by Mandal et al. in oxalic acid [44], Kang et al. in aqueous H_3PO_4 [45], and Rafiei et al. in Kalling's reagent [46], established that the etching of IN718, either chemical or electrochemical, is performed with a solitary motive to investigate the microstructures, grain structures, and precipitates under the optical microscopes. To the best of our knowledge, anisotropic or isotropic etching of IN718 has not been discussed in the literature and requires particular attention. In principle with the mechanism, isotropic etching polishing is based on the merging of isotropic etching holes formed on the IN718 surface after the breakdown of the passivation layer. Besides, the anisotropy of IN718 etching is dependent upon the electrolyte concentration, temperature, and applied electric potential. The anisotropy of the IN718 etching studied at room temperature based on the electrolyte concentration is shown in Fig. 6.

Table 2
Chemical composition of the passivated IN718 measured by EDS.

Element	Ni	Cr	Fe	Nb	Mo	Ti	Al	O
IN718 (wt%)	50.82	24.9	18.2	2.63	1.55	0.39	0.32	1.15

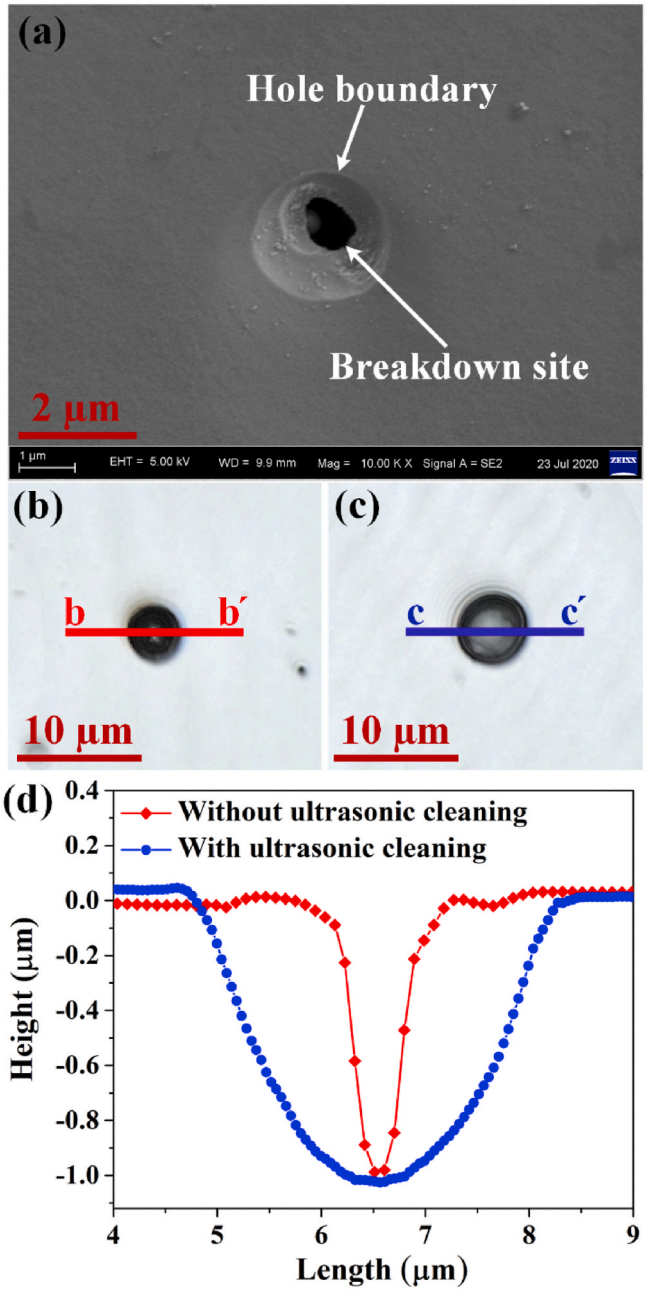

Fig. 5. Passivation layer breakdown site images of the IN718 etched at 0.3 A for 80 s in electrolytes having 20 ml H_2SO_4 concentration in 100 ml methanol without ultrasonic cleaning, SEM image (a), LSCM image without ultrasonic cleaning (b), LSCM image with ultrasonic cleaning (c), and LSCM cross-sectional profiles of the etching sites without and with ultrasonic cleaning (d).

As discussed, IN718 used in this study has precipitated γ phase (FCC, a = 3.591 Å), γ″ phase (BCT, a = 3.624 Å, c = 7.406 Å), and MC carbides (Cubic, a = 4.30–4.70 Å), the lattice parameters are taken from Nunes et al. [47]. These crystallographic phases have different faces, such as (111), (200), and (220), as confirmed by the XRD analysis. The crystal structures and the crystallographic faces of the γ and γ″ phase are shown in Fig. 6(a) and (b), respectively. The anisotropic etching holes formed on the IN718 substrate surface during etching at 0.05 A in an electrolyte having 1 ml H_2SO_4 concentration in 100 ml methanol are shown in Fig. 6

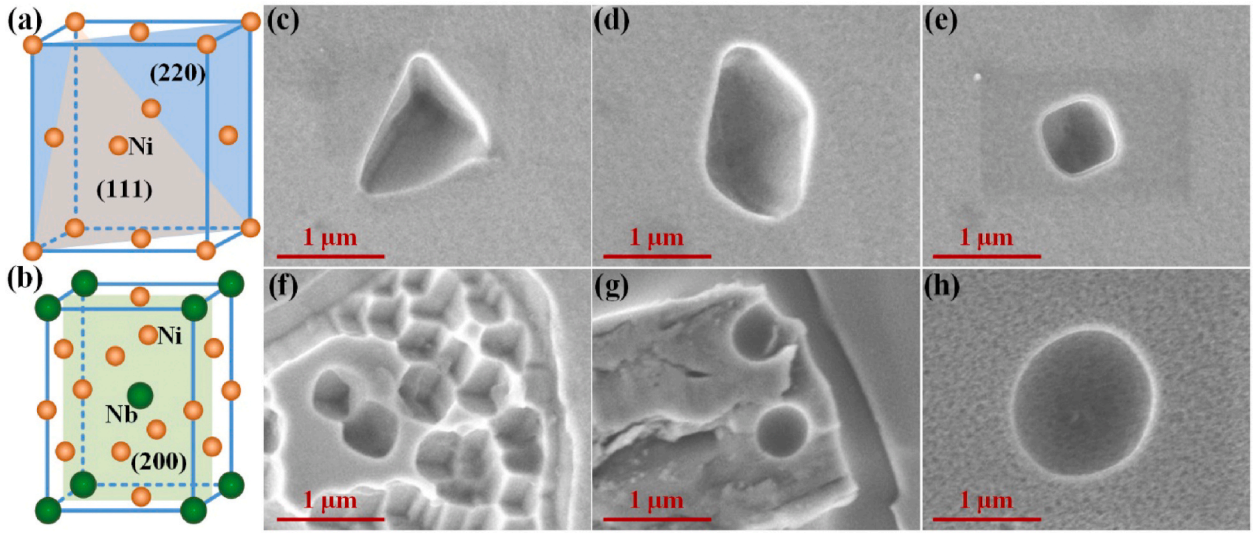

Fig. 6. Crystal structure of γ phase (a) and γ″ phase (b); and the morphology of etching holes formed on the IN718 substrate after etching at 0.05 A for 80 s in electrolytes with 1 ml (c–f), and 20 ml (g–h) H_2SO_4 concentration in 100 ml methanol.

(c–f). For 1 ml H_2SO_4 concentration in 100 ml methanol, the supply of the H_2SO_4 to the crystallographic faces depends upon their orientations relative to the substrate, therefore, unlike dissolution rates due to the inhomogeneous supply of H_2SO_4 resulted in the odd dissolution of these faces and the formation of anisotropic etching holes. Ling and Starke Jr [48] performed the thermal etching of β-Ti-V alloys and reported the formation of anisotropic etching holes on the metal surface, attributing them to the presence of different crystallographic faces. Similarly, phase-dependent dissolution and the formation of anisotropic and isotropic etching holes on and the α + β double phase Zr alloy and single-phase β-Zr alloy, respectively, was also reported [49]. However, keeping other conditions such as etching current, temperature, and duration as constant, and increasing H_2SO_4 concentration to 20 ml in 100 ml methanol resulted in the homogeneous dissolution of crystallographic faces, ultimately forming isotropic etching holes irrespective of the phases and MC carbides, as shown in Fig. 6(g and h). The formation of the isotropic etching holes at higher H_2SO_4 concentration in methanol is positively related to the abundant supply of H_2SO_4 (SO_4^{2-}acceptor ions) to all the faces, that is why the etching becomes independent of face direction and dissolution rates.

To further investigate the etching anisotropy, IN718 was also etched at 0.05 A for 80 s in an electrolyte having 20 ml H_2SO_4 concentration in 100 ml methanol at different temperatures such as 5, 15, 45, and 65 °C, as shown in Fig. 7. The desired electrolyte temperature was maintained by keeping the reaction cell in a temperature-controlled thermostat circulator (Laboto, CC-2008EW), having a temperature range of −20 to 100 °C. After achieving desired electrolyte temperature, the IN718 substrate was immersed in the electrolyte, and the whole system was kept at the same temperature for 5 min to develop an equilibrium state before etching. It was observed that the etching performed below room temperature (at 5 and 15 °C) is anisotropic, as shown in Fig. 7(a and b). The anisotropy is caused by the increasing viscosity of the electrolyte below room temperature. The viscosity of the electrolyte has a direct influence on the transportation of the acceptor ions SO_4^{2-}that coordinate with the metal ions (Ni, Cr, Ti, etc.) on the metal surface and carry them away. Therefore, the limited transportation of the acceptor ions at low temperatures results in the shortage of $SO_4^{2-}$to different crystallographic faces, subsequently resulting in the anisotropic etching. However, etching performed above room temperature (at 45 and 65 °C) is isotropic with no significant effect on the shape of etching holes, as shown in Fig. 7(c and d). Therefore, further experiments were conducted at room temperature in an electrolyte having 20 ml H_2SO_4 concentration

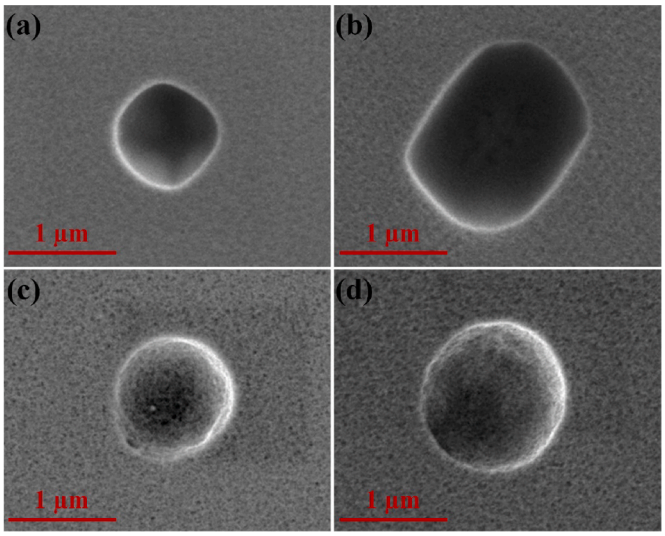

Fig. 7. Morphologies of etching holes formed on the IN718 substrate after etching at 0.05 A for 80 s in electrolytes with 20 ml H_2SO_4 concentration in 100 ml methanol at different electrolyte temperatures 5 °C (a), 15 °C (b), 45 °C (c), and 65 °C (d).

in 100 ml methanol, and the corresponding electrolyte hereafter will be denoted as 20:100H_2SO_4 electrolyte.

It has been well established that forming isotropic hemispheric holes on the IN718 substrate through isotropic etching in 20:100H_2SO_4 electrolyte is experimentally feasible. However, the merging of isotropic etching holes is necessary to obtain a smooth and uniform polished surface, which is associated with the growth of hole diameter and density. Therefore, the isotropic etching was systematically performed in 20:100H_2SO_4 electrolytes for 80 s at different etching currents 0.05, 0.1, 0.2, 0.3, 0.4, and 0.5 A to study the evolution of etching hole density on the IN718 substrate, as shown in Fig. 8. At a low current up to 0.1 A, very few etching holes with smaller diameter could be realized on the substrate, which might be due to the low current density. Further increasing etching current from 0.2 to 0.3 A increased both the diameter and density of the etching holes, while merging of the isotropic etching holes could also be observed at arbitrary positions. The formation of the etching holes is related to the spontaneous breakdown of the passivation

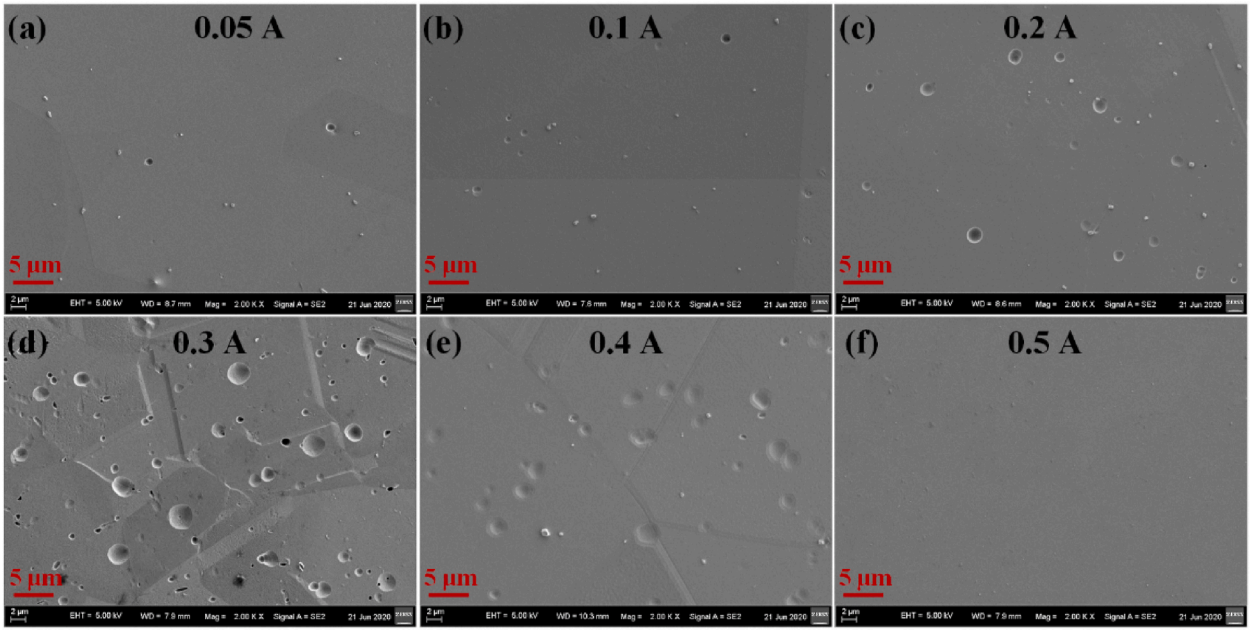

Fig. 8. Surface morphologies of IN718 after IEP in 20:100H_2SO_4 electrolytes for 80 s at different etching currents.

layer, depending on the layer thickness and the applied current. At 0.4 A, on the one hand, the nearby etching holes merged that increased the size of the etched substrate surface area, while on the other side, the depths of the etching holes became shallow, and the polishing effect started appearing. Rapid merging of etching holes and the occurrence of polishing effect might be related to the increasing MRR that shallowed

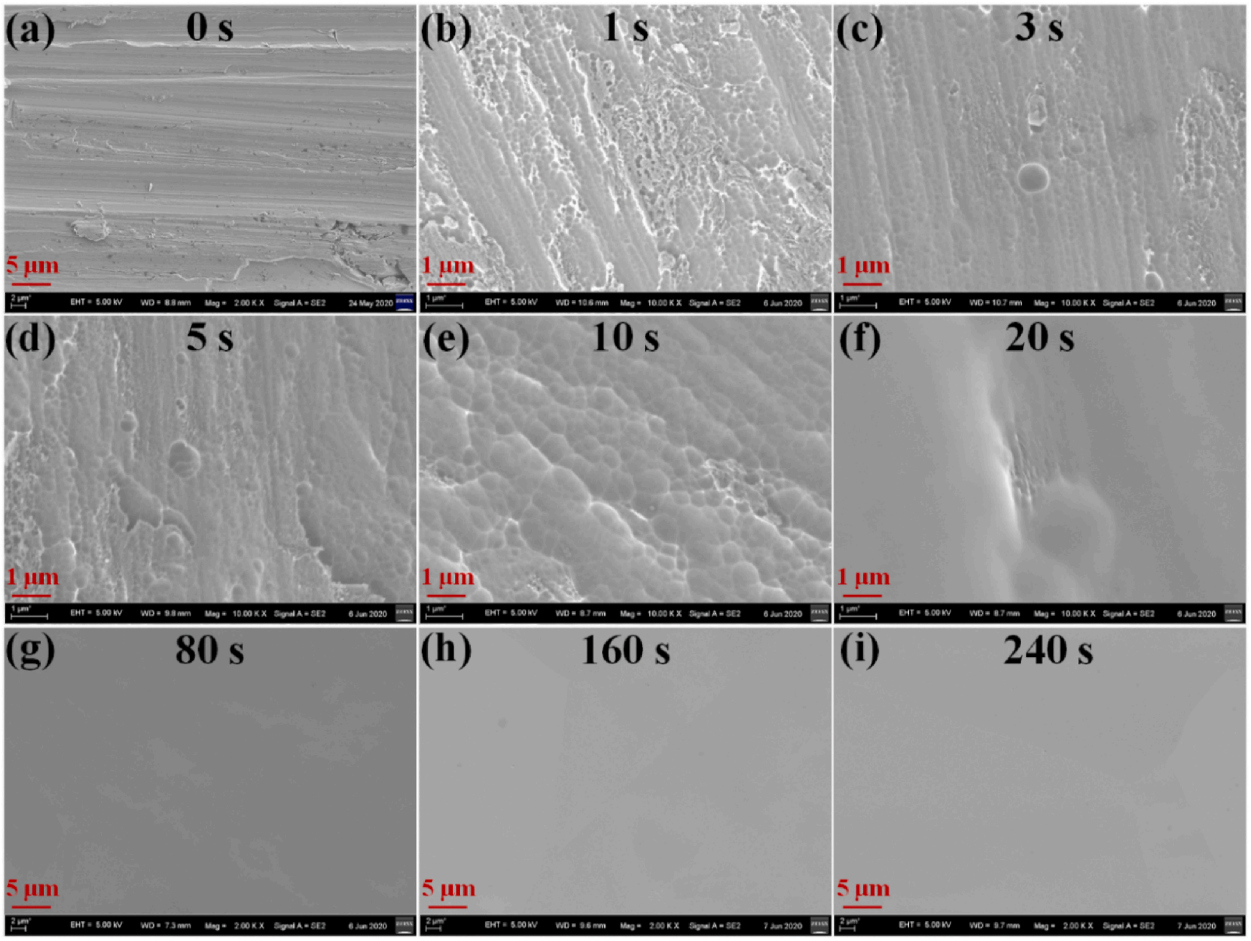

Fig. 9. Surface morphologies of IN718 after IEP in 20:100H_2SO_4 electrolytes at 0.8 A for different etching durations.

the depths of the etching holes at high etching current. Further increasing the etching current to 0.5 A resulted in the polished surface, which also suggests using high current densities for smooth and rapid finishing of the IN718 substrate surface.

3.4. Polishing characteristics of IEP of IN718

Referring to the discussion about etching anisotropy and surface morphologies of the IN718 under different etching currents, the surface evolution and variation in the Sa roughness of the IN718 were studied as a function of the etching duration. The morphology of the IN718 sample after finely grounding with a wet 600-grit SiC sandpaper is shown in Fig. 9(a). The surface morphologies of the IN718 etched at 0.8 A in 20:100H_2SO_4 electrolytes for different durations 1, 3, 5, 10, 20, 80, 160, 240 s are shown in Fig. 9(b–i). After being etched for 1 s, although many etching holes emerged on the surface of the substrate, the sharpness of the wet grounding marks still can be seen. After being etched up to 5 s, the etching holes grew up in different sizes, while some isotropic etching holes with large diameters were also spotted on the IN718 surface. The discrepancies among the diameters of the etching holes are due to the random breakdown of the passivation layer at arbitrary positions. Moreover, delicate signs of wet grounding marks were still observed on the IN718 surface. After etching for 10 s, the extensive merging of isotropic etching holes was observed, while large scale polishing effects were visible after 20 s with a piddling residual area. Subsequently, the polishing effects further improved with the increasing etching duration, and clear grain boundaries could be seen for 160 and 240 s without any indication of asymmetric dissolution, as shown in Fig. 9(h and i).

The Sa roughness is determined by the following expression [26]:

$$Sa = \frac{1}{n}\sum_{1}^{n}\left|Z_k - \overline{Z}\right| \quad (5)$$

where $Z_k$presents the distance of the measured surface from the mean plane$\overline{Z}$. A sharpened tetrahedral shaped silicon AFM tip (OMCL-AC160TS) having 7 nm radius and 300 (±100) kHz resonance frequency is used to physically probe the surface over an area of 10 × 10 μm^2, while 3rd order image flattening was applied before roughness measurement. Variation in the Sa roughness of the IN718 surface as a function of the etching duration is presented in Fig. 10(a). Initially, the Sa roughness of the IN718 kept increasing with the etching duration up to 10 s. Comparing Fig. 9(b–e) with Fig. 10 for etching duration varying from 0 to 10 s, it can be seen that the increasing Sa roughness (Sa = 23.9–72.3 nm) is strongly correlated to the formation of etching holes on the surface. The etching holes formed after the passivation layer breakdown increased the surface roughness beyond the initial value, which is consistent with the mechanism of the IEP discussed in Yi et al. [26]. However, a large decrease in the Sa roughness (Sa = 72.3–13.9 nm) after 20 s etching is due to the pronounced polishing effect that appeared after the merging of etching holes on the surface. Eventually, the Sa roughness decreased gradually with increasing etching duration to 240 s, ultimately polishing off at Sa = 1.11 nm. Besides, Sa roughness profiles of the IN718 surface measured by AFM before and after IEP are also shown in Fig. 10(b) and c, respectively. It can be concluded that the surface morphology and variation in the Sa roughness are consistent with each other and imitate the mechanism of IEP reported in Ref. [26].

As discussed, high etching current is preferred for the efficient finishing of a highly rough surface, therefore the IEP of a comparatively rougher IN718 has also been carried at 3A for 300 s in 20:100H_2SO_4 electrolyte, as shown in Fig. 11. The morphology of the IN718 surface finely grounding with a wet 180-grit SiC sandpaper is shown in Fig. 11 (a). The surface morphology of uniformly smoothed IN718 after IEP at 3 A for 300 s in 20:100H_2SO_4 electrolyte is shown in Fig. 11(b). Apart from very few tiny carbides, the rough IN718 surface is transformed into a smooth and shiny surface regardless of the different phases. The AFM images of the surface roughness and surface sectional profiles of both

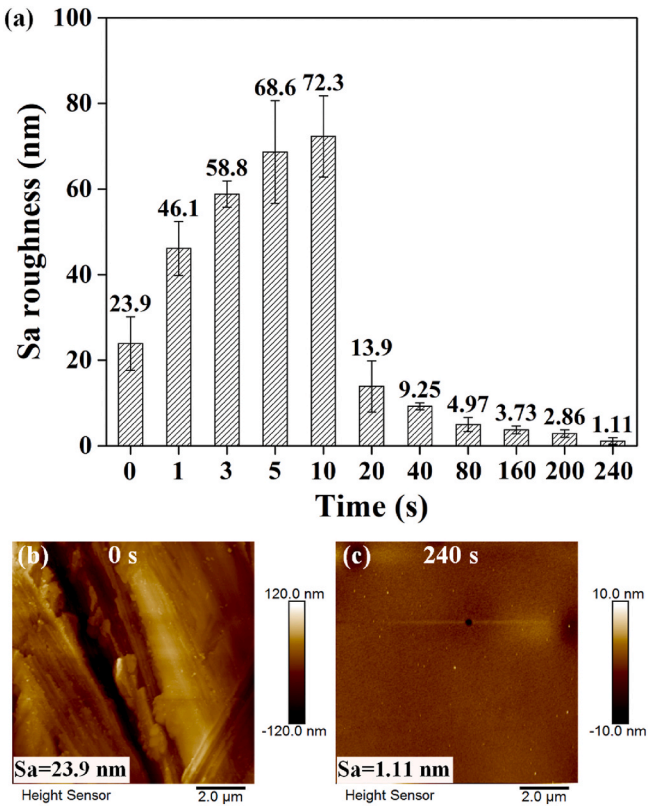

Fig. 10. Variation in the Sa roughness of IN718 with IEP in 20:100H_2SO_4 electrolytes at 0.8 A for different durations (a), surface profiles of IN718 by AFM, before (b), and after (c).

wet grounded and IEP-processed surfaces are also shown in Fig. 11(c–f), which shows that the Sa r(h)oughness has been drastically decreased from 62.7 nm to 0.86 nm after IEP for 300 s. Atomic and close-to-atomic scale manufacturing (ACSM) is a futuristic industrial technique that involves direct processing of atoms [50,51]. The obtained sub-nanometer surface roughness of IN718 proposes IEP an alternative ACSM technique, which can be used for high added value manufacturing. The transformation of a highly rough surface to a mirror-like polished surface by isotropic etching can be seen in Fig. 11(g and h). As discussed, the backend of IN718 substrate is covered with a Teflon sample holder, therefore the substrate is rarely polished from the back. Besides, no significant edge rounding or change in the substrate diameter is observed after 300 s of polishing at 3 A in 20:100H2SO4 electrolyte, as shown in Fig. 11(h).

The material removal rate is an important parameter extracted from the basic experimental data to define the efficiency of polishing techniques. The MRR of IN718 during IEP in 20:100H_2SO_4 electrolytes at different etching currents and durations are shown in Fig. 12(a) and (b), respectively. It can be observed that the MRR increases almost linearly with increasing etching current, and the highest MRR = 2.73 mm^3/min suggests a rapid and highly efficient IEP mechanism at 3 A. Increasing MRR with etching current is related to the intensified production of the ions and their high mobility. Besides, the MRR with etching duration first decreased significantly and then became almost consistent. Initially, the MRR is higher due to the rapid formation of etching holes and the dissolution of protrudes, signifying macro polishing. However, after 10 s etching at 3 A in 20:100H_2SO_4 electrolyte, the formation and merging of etching holes reduced significantly due to the apparent polishing effects. Other than the deterioration of electrolyte after a longer polishing duration, the substrate also turned to be an equipotential surface with only micro polishing occurring on the surface.

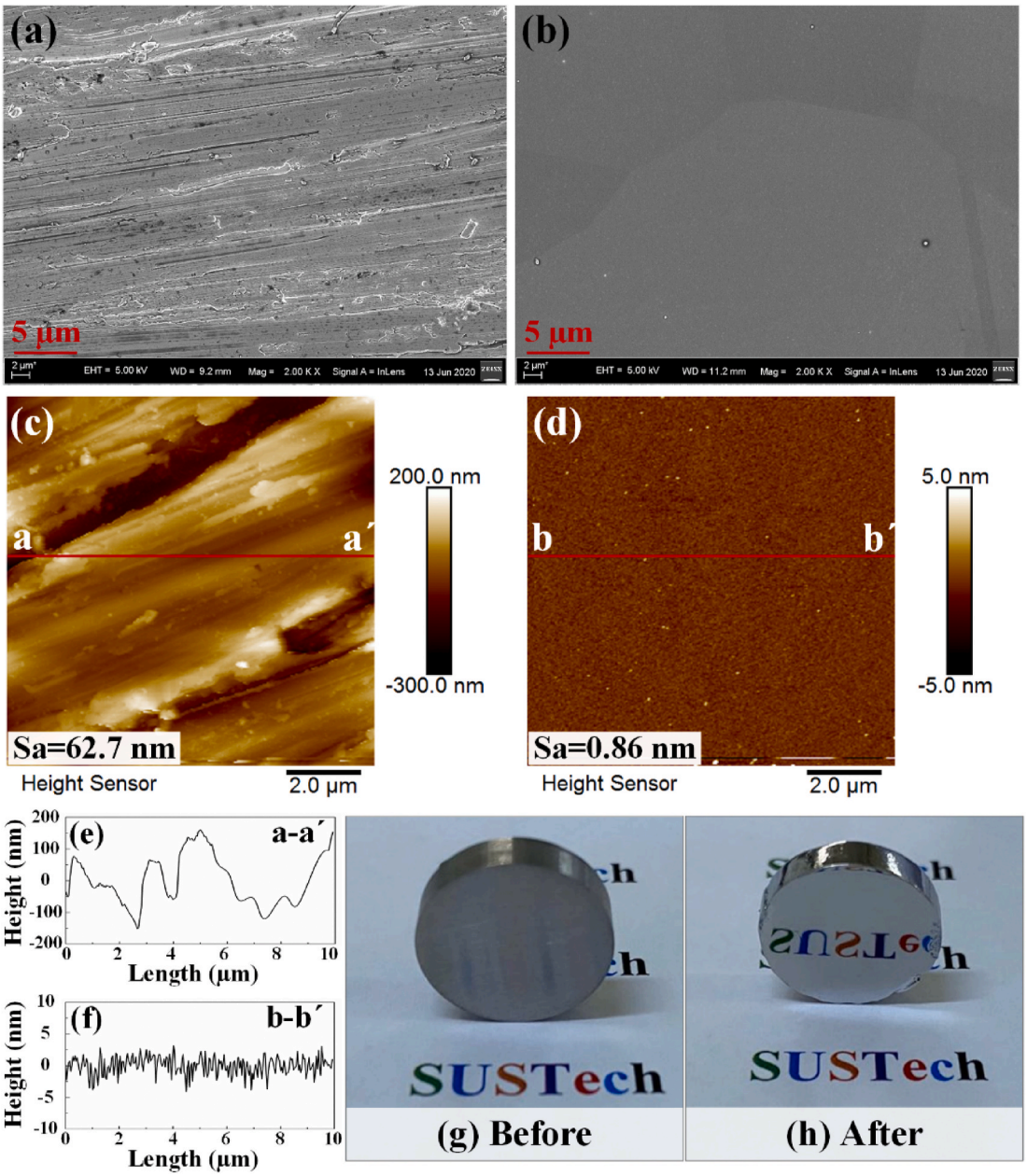

Fig. 11. Surface morphologies, Sa roughnesses and surface profiles by AFM, and pictures of IN718 before (a, c, e, and g) and after 300 s of IEP at 3 A in 20:100H_2SO_4 electrolytes (b, d, f, and h).

4. Summary

The polishing of nickel alloy IN718 precipitated with γ and γ″ phase, and MC carbides is quite challenging because of the different chemical and mechanical properties of each phase. This paper has focused on the effect of electrolyte concentration and temperature on the etching isotropy and the characteristics of isotropic etching polishing of IN718 in the H_2SO_4 electrolyte. The material properties, potentiodynamic behaviors, and etching anisotropy of IN718 were investigated. The polishing characteristics of the IEP of IN718 were presented. Based on the experimental findings, the key conclusions are as follows:

(1) The potentiodynamic measurements in different electrolytes exhibit similar cathodic, passive, and transpassive regions, especially the second passivation of IN718. According to the Tafel plot measurements, increasing the concentration of H_2SO_4 in methanol decreases the value of the limiting current, and the least limiting current density was recorded for 30 ml H_2SO_4 concentration in 100 ml methanol. Moreover, the corrosion resistance of IN718 increased with increasing H_2SO_4 concentration in methanol.

(2) IN718 is a multiphase alloy (γ, γ″) with different crystallographic faces that result in etching anisotropy due to odd electrochemical dissolution. The electrolyte concentration and temperature can modulate the etching anisotropy of IN718. While it is anisotropically etched in an electrolyte with 1 ml H_2SO_4 concentration in 100 ml methanol, the etching becomes isotropic in an electrolyte with 20 ml H_2SO_4 concentration in 100 ml methanol regardless of the crystallographic phases and MC carbides. The etching also transformed from anisotropic to isotropic with electrolyte temperature rising to or above the room temperature.

(3) The density of the etching holes increased with the etching current resulting in the rapid polishing effect. The surface evolution of IN718 during IEP at 0.8 A shows that the surface roughness

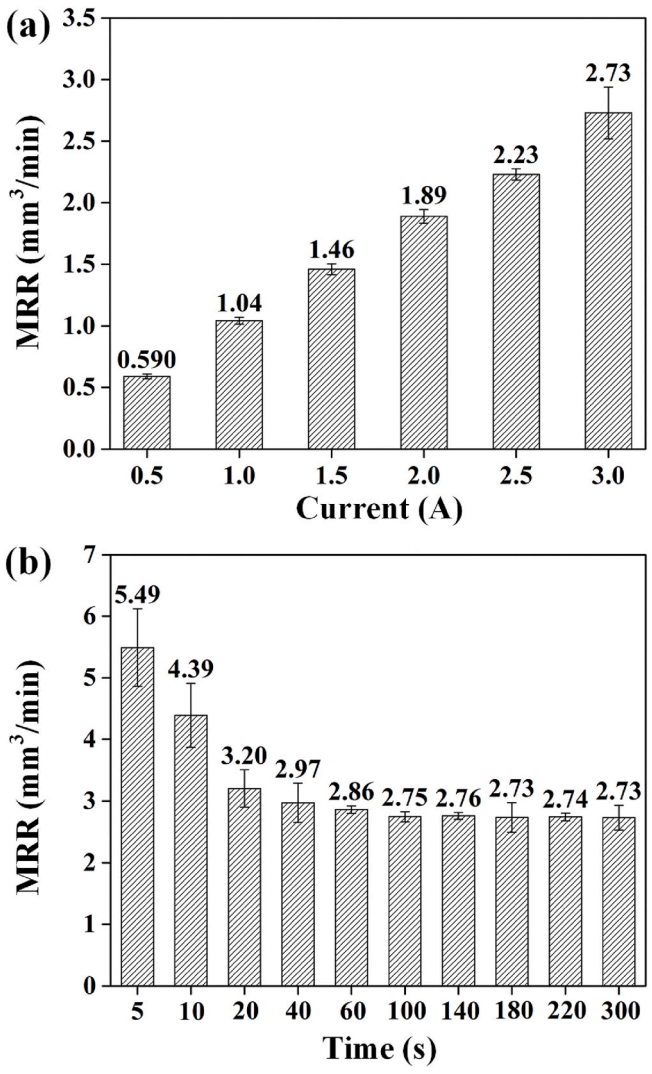

Fig. 12. Material removal rates of IN718 in 20:100H_2SO_4 electrolytes, etching for 300 s at different etching currents (a), and etching at 3 A for different etching durations (b).

first increased due to the formation of etching holes, then decreased abruptly with the rapid merging of etching holes, and finally achieved a smooth surface.

(4) The wet grounded surface of IN718 was transformed into a mirror-like smooth surface after 300 s of IEP at optimized conditions. The Sa roughness drastically dropped from 62.7 nm to 0.86 nm with an MRR of 2.73 mm^3/min.

The preceding experimental results demonstrate IEP as a generic technique for polishing flat surfaces. In the future, the IEP is anticipated to polish 3D printed IN718 intricate geometries used in the aero-industry.

Declaration of competing interest

The authors declare that they have no known competing financial interests or personal relationships that could have appeared to influence the work reported in this paper.

Acknowledgments

This project is supported by National Natural Science Foundation of China (Grant No. 52035009, 52005243), the research fund for International Cooperation (GJHZ20180928155412525), and the Shenzhen High-level Innovation and Entrepreneurship Fund (No. KQTD20170810110250357) from the Science and Technology Innovation Committee of Shenzhen Municipality, Shenzhen, China. The authors acknowledge the assistance of SUSTech Core Research Facilities.

References

[1] Ulutan D, Ozel T. Machining induced surface integrity in titanium and nickel alloys: a review. Int J Mach Tool Manufact 2011;51:250–80.
[2] Du JH, Lu XD, Deng Q, Qu JL, Zhuang JY, Zhong ZY. High-temperature structure stability and mechanical properties of novel 718 superalloy. Mater Sci Eng, A 2007; 452–453:584–91.
[3] Sharman A, Hughes J, Ridgway K. Workpiece surface integrity and tool life issues when turning Inconel 718™ nickel based superalloy. Mach Sci Technol 2004;8. 399-14.
[4] Scharfrik R, Sprague R. The saga of gas turbine materials, Part III. Adv Mater Process 2004;162:33–5.
[5] Ren X, Liu Z. Influence of cutting parameters on work hardening behavior of surface layer during turning superalloy Inconel 718. Int J Adv Manuf Technol 2016;86:2319–27.
[6] Li Y, Wu Y, Zhou L, Fujimoto M. Vibration-assisted dry polishing of fused silica using a fixed-abrasive polisher. Int J Mach Tool Manufact 2014;77. 93-02.
[7] Tsai M-Y, Yang W-Z. Combined ultrasonic vibration and chemical mechanical polishing of copper substrates. Int J Mach Tool Manufact 2012;53:69–76.
[8] Meng F, Zhang Z, Gao P, Liu T, Boyjoo Y, Guo D. Design of composite abrasives and substrate materials for chemical mechanical polishing applications. Appl Nanosci 2020;10:1379–93.
[9] Bhattacharyya B, Doloi B. Modern machining Technology: advanced, hybrid, micro machining and super finishing Technology. Academic Press; 2019.
[10] Wang CJ, Cheung CF, Ho LT, Liu MY, Lee WB. A novel multi-jet polishing process and tool for high-efficiency polishing. Int J Mach Tool Manufact 2017;115:60–73.
[11] Deng T, Li J, Zheng Z. Fundamental aspects and recent developments in metal surface polishing with energy beam irradiation. Int J Mach Tool Manufact 2020; 148:103472.
[12] Singh AK, Jha S, Pandey P. Nanofinishing of a typical 3D ferromagnetic workpiece using ball end magnetorheological finishing process. Int J Mach Tool Manufact 2012;63:21–31.
[13] Gao Y-k. Surface modification of TC4 titanium alloy by high current pulsed electron beam (HCPEB) with different pulsed energy densities. J Alloys Compd 2013;572:180–5.
[14] Holmberg J, Berglund J, Wretland A, Beno T. Evaluation of surface integrity after high energy machining with EDM, laser beam machining and abrasive water jet machining of alloy 718. Int J Adv Manuf Technol 2019;100:1575–91.
[15] Bordatchev EV, Hafiz AMK, Tutunea-Fatan OR. Performance of laser polishing in finishing of metallic surfaces. Int J Adv Manuf Technol 2014;73:35–52.
[16] Zhihao F, Libin L, Longfei C, Yingchun G. Laser polishing of additive manufactured superalloy. Procedia CIRP 2018;71:150–4.
[17] Krishnan A, Fang FZ. Review on mechanism and process of surface polishing using lasers. Front Mech Eng 2019:1–21.
[18] Han W, Fang FZ. Fundamental aspects and recent developments in electropolishing. Int J Mach Tool Manufact 2019;139:1–23.
[19] Qin S, Deng H. Electrochemical etching of tungsten for fabrication of sub-10-nm tips with a long taper and a large shank. Nanomanufact Metrol 2019;2:235–40.
[20] Gomez-Gallegos A, Mill F, Mount AR. Surface finish control by electrochemical polishing in stainless steel 316 pipes. J Manuf Process 2016;23:83–9.
[21] Tailor PB, Agrawal A, Joshi SS. Evolution of electrochemical finishing processes through cross innovations and modeling. Int J Mach Tool Manufact 2013;66: 15–36.
[22] Huang C, Chen Y, Chang JH. The electrochemical polishing behavior of the Inconel 718 alloy in perchloric–acetic mixed acids. Corrosion Sci 2008;50:480–9.
[23] Yang X, Yang X, Sun R, Kawai K, Arima K, Yamamura K. Obtaining atomically smooth 4H–SiC (0001) surface by controlling balance between anodizing and polishing in electrochemical mechanical polishing. Nanomanufact Metrol 2019;2: 140–7.
[24] Jacquet P. The mechanism of electrolytic polishing of Copper. C R Acad Sci 1936; 202:402.
[25] Mount AR, Howarth PS, Clifton D. The electrochemical machining characteristics of stainless steels. J Electrochem Soc 2003;150:D63.
[26] Yi R, Zhang Y, Zhang X, Fang F, Deng H. A generic approach of polishing metals via isotropic electrochemical etching. Int J Adv Manuf Technol 2020;50:103517.
[27] Rotty C, Mandroyan A, Doche M-L, Hihn Y. Electropolishing of CuZn brasses and 316L stainless steels: influence of alloy composition or preparation process (ALM vs. standard method). Surf Coating Technol 2016;307:125–35.
[28] Gribbin S, Ghorbanpour S, Ferreri NC, Bicknell J, Tsukrov I, Knezevic M. Role of grain structure, grain boundaries, crystallographic texture, precipitates, and porosity on fatigue behavior of Inconel 718 at room and elevated temperatures. Mater Char 2019;149:184–97.
[29] Ghorbanpour S, Alam ME, Ferreri NC, Kumar A, McWilliams BA, Vogel SC, Bicknell J, Beyerlein IJ, Knezevic M. Experimental characterization and crystal plasticity modeling of anisotropy, tension-compression asymmetry, and texture evolution of additively manufactured Inconel 718 at room and elevated temperatures. Int J Plast 2020;125:63–79.

[30] Special metals. https://www.americanspecialmetals.com/inconelalloy718.html. [Accessed 10 October 2020].
[31] Mostafa A, Picazo Rubio I, Brailovski V, Jahazi M, Medraj M. Structure, texture and phases in 3D printed IN718 alloy subjected to homogenization and HIP treatments. Metals 2017;7:196.
[32] Chamanfar A, Sarrat L, Jahazi M, Asadi M, Weck A, Koul AK. Microstructural characteristics of forged and heat treated Inconel-718 disks. Mater Des 2013;52:791–800.
[33] Wang C, Li R. Effect of double aging treatment on structure in Inconel 718 alloy. J Mater Sci 2004;39:2593–5.
[34] Goodfellow AJ. Strengthening mechanisms in polycrystalline nickel-based superalloys. Mater Sci Technol 2018;34. 1793-08.
[35] Reggiani RC, Mazza F, Sivieri E. Electrochemical polishing of titanium in perchloric-methanolic solutions. Mater Chem 1979;4:149–58.
[36] Singh VB, Gupta A. Active, passive and transpassive dissolution of In-718 alloy in acidic solutions. Mater Chem Phys 2004;85:12–9.
[37] Myers JR, Beck F, Fontana MG. Anodic polarization behavior of nickel-chromium alloys in sulfuric acid solutions. Corrosion 1965;21:277–87.
[38] Bojinov M, Fabricius G, Kinnunen P, Laitinen T, Mäkelä K, Saario T, Sundholm G. The mechanism of transpassive dissolution of Ni–Cr alloys in sulphate solutions. Electrochim Acta 2000;45. 2791-02.
[39] Sikora E, Macdonald DD. Nature of the passive film on nickel. Electrochim Acta 2002;48:69–77.
[40] Chaudhary RS, Singh A. Technical note: transpassive anodic dissolution ofnickel in sulphuric acid. Br Corrosion J 1993;28:227–9.
[41] Cunha L, Andritschky M, Rebouta L, Pischow K. Corrosion of CrN and TiAlN coatings in chloride-containing atmospheres. Surf Coating Technol 1999;116:1152–60.
[42] Mishra A. Performance of corrosion-resistant alloys in concentrated acids. Acta Metall Sin 2017;30(4):306–18.
[43] Giggins C, Pettit FS. Oxidation of Ni-Cr-Al alloys between 1000° and 1200°C. J Electrochem Soc 1971;118:1782.
[44] Mandal P, Lalvani H, Tuffs M. Cold rotary forging of Inconel 718. J Manuf Process 2019;46:77–99.
[45] Kang Y-J, Yang S, Kim Y-K, AlMangour B, Lee K-A. Effect of post-treatment on the microstructure and high-temperature oxidation behaviour of additively manufactured Inconel 718 alloy. Corrosion Sci 2019;158:108082.
[46] Rafiei M, Mirzadeh H, Malekan M. Micro-mechanisms and precipitation kinetics of delta (δ) phase in Inconel 718 superalloy during aging. J Alloys Compd 2019;795:207–12.
[47] Nunes RM, Pereira D, Clarke T, Hirsch TK. Delta phase characterization in Inconel 718 alloys through X-ray diffraction. ISIJ Int 2015;55:2450–4.
[48] Ling F-W, Starke Jr EA. Thermal etching of β Ti-V alloys. Metallography 1972;5.399-07.
[49] Xia C, Feng Z, Liu S, Zhang X, Zhang B, Pan B, Zhang X, Ma M, Liu R. Anisotropic pitting of single-phase β-Zr alloy and isotropic pitting of α + β double-phase Zr alloy. Corrosion Sci 2017;127:39–44.
[50] Mathew PT, Rodriguez BJ, Fang F. Atomic and close-to-atomic scale manufacturing: a review on atomic layer removal methods using atomic force microscopy. Nanomanufact Metrol 2020:1–20.
[51] Fang F. Atomic and close-to-atomic scale manufacturing: perspectives and measures. Int J Extrem Manuf 2020;2:030201.